nature materials

Article

https://doi.org/10.1038/s41563-023-01476-6

An ordered, self-assembled nanocomposite with efficient electronic and ionic transport

Received: 22 August 2022

Accepted: 11 January 2023

Check for updates

Tyler J. Quill[1], Garrett LeCroy[1], David M. Halat[2,3], Rajendar Sheelamanthula[4], Adam Marks[1], Lorena S. Grundy[2,3], Iain McCulloch[4,5], Jeffrey A. Reimer[2,3], Nitash P. Balsara[2,3], Alexander Giovannitti[1] ✉, Alberto Salleo[1] ✉ & Christopher J. Takacs[6] ✉

Mixed conductors—materials that can efficiently conduct both ionic and electronic species—are an important class of functional solids. Here we demonstrate an organic nanocomposite that spontaneously forms when mixing an organic semiconductor with an ionic liquid and exhibits efficient room-temperature mixed conduction. We use a polymer known to form a semicrystalline microstructure to template ion intercalation into the side-chain domains of the crystallites, which leaves electronic transport pathways intact. Thus, the resulting material is ordered, exhibiting alternating layers of rigid semiconducting sheets and soft ion-conducting layers. This unique dual-network microstructure leads to a dynamic ionic/electronic nanocomposite with liquid-like ionic transport and highly mobile electronic charges. Using a combination of operando X-ray scattering and in situ spectroscopy, we confirm the ordered structure of the nanocomposite and uncover the mechanisms that give rise to efficient electron transport. These results provide fundamental insights into charge transport in organic semiconductors, as well as suggesting a pathway towards future improvements in these nanocomposites.

Mixed conduction—the ability to simultaneously transport both electronic and ionic species—is crucial for a wide array of current and emerging technologies[1], and mixed conductors can be considered a separate and important class of solids, next to metals, insulators, semiconductors and ionic conductors. More specifically, there is great interest in solid-state materials where fast ionic-concentration changes can deeply modulate the electronic and optical properties on timescales commensurate with modern electronics requirements[2]. The transport of ions and electrons, however, imposes somewhat antithetical requirements on solids, making it difficult to obtain materials that perform both functions well. Critically, there is a lack of fundamental understanding regarding how the coupled dynamics between ions and electrons can be co-designed to promote efficient transport and novel properties for both charged species compared with pure electronic and ionic conductors. As a result, phase-separated composites[3–5], conjugated polymer/polyelectrolyte blends[6,7] or electrically conductive additives mixed into ionic conductors[8,9] are often used; however, this is far from optimal as it directly results in lower charge densities. For example, metal-oxide cathode materials for battery applications require conductive additives to enhance the electronic conductivity for ion intercalation. The ability to synthesize such composites at the mesoscale and nanoscale is a longstanding grand challenge, where the large number of interfaces per unit volume is functional to obtain high charge densities[1,4].

[1]Department of Materials Science and Engineering, Stanford University, Stanford, CA, USA. [2]Department of Chemical and Biomolecular Engineering and College of Chemistry, University of California, Berkeley, CA, USA. [3]Materials Sciences Division and Joint Center for Energy Storage Research, Lawrence Berkeley National Laboratory, Berkeley, CA, USA. [4]Physical Science and Engineering Division, King Abdullah University of Science and Technology (KAUST), Thuwal, Saudi Arabia. [5]Department of Chemistry, University of Oxford, Oxford, UK. [6]Stanford Synchrotron Radiation Lightsource, SLAC National Accelerator Laboratory, Menlo Park, CA, USA. ✉e-mail: asalleo@stanford.edu; ag19@stanford.edu; ctakacs@slac.stanford.edu

Organic polymer mixed ionic/electronic conductors (OMIECs) are an emerging class of materials with promise in a wide range of electrochemical devices for energy storage[10], bioelectronics[11] and neuromorphic computing[12]. Although the vast majority of OMIEC literature uses aqueous electrolytes[13], their use with ionic liquids opens opportunities to tailor ionic and electronic functionalities[14]. Ionic liquids—molten salts of charged species without a solvent—have become known as designer electrolytes owing to the ability to synthetically tune the physiochemical properties of these molecules[15]. Although these molecules can induce phase separation in conjugated polymer/polyelectrolyte blends[16,17], we find that with a judicious choice of materials, ionic liquids spontaneously incorporate into conjugated polymer crystallites as neutral pairs[18]. This infiltration is spontaneous only when the side chains are designed to be solvated by the ionic liquid. The resulting material is a veritable composite consisting of liquid-like ionically conducting lamellae and semirigid electronically conducting lamellae, both structured at the nanoscale and essentially behaving as a single material as if it were a compound.

The mixed-conductor nanocomposite presents unique advantages compared with its inorganic counterparts. The self-assembly of the organic semiconductor into lamellae is spontaneously achieved at the nanoscale to provide high volumetric charge densities without the need for the elaborate processing techniques typically required to structure inorganic materials at comparable length scales[4]. We find that the semiconductor lamellae template the nanocomposite formation at the molecular scale as ion swelling occurs only in the softer side-chain domains of the polymer crystallites, preserving this layered structure and leaving the more rigid pathways of electronic transport unperturbed. As a result of this templated self-assembly, ionic and electronic transport pathways coexist within the same unit cell with intimate contact and still enable the efficient conduction of both species simultaneously. This self-assembled nanostructure enables changes in ion composition under an external potential with minimal structural perturbation to the electronically conducting domains, which enables us to investigate how electronic charge carriers affect the ordering of the semiconductor. Importantly, ionic conduction is also efficient at room temperature owing to the liquid-like nature of the ionic domains. Thus, the molecularly templated structure combined with the highly anisotropic nature of transport and volumetric doping of OMIECs simultaneously leads to optimal ionic and electronic transport properties. In addition to the energy storage and electrocatalysis space, the ionic and electronic transport properties of this nanocomposite opens the applications of electrochemical materials in the microelectronics space, where iontronics have recently attracted much attention[2,19,20]. Finally, the wide materials space available for exploration on both semiconductor side and ionic-liquid side promises much room for improvement and exploration of different application areas.

To inform the synthetic design of these promising nanocomposites for future applications, a fundamental understanding of the charging and transport in these materials must first be established. To date, however, microstructural changes during OMIEC operation are largely unknown. Indeed, despite notable progress[21–26], simultaneously measuring carrier density and conductivity as well as characterizing structural changes (for example, by grazing-incidence X-ray scattering) has proven to be challenging. Thus, studies providing mechanistic insights and rigorous structure–property relationships have been limited. To fill this gap, we developed operando measurements that quantify structural changes during electrochemical charging and correlate the evolving microstructure to the simultaneously measured electronic transport properties (such as hole mobility). We use these insights to reveal which semiconductor microstructure is the most favourable for charge transport, thereby suggesting a path towards future improvements in these nanocomposites.

Monitoring structure with operando X-ray scattering

To study the paired electrical and structural dynamics in the mixed-conductor nanocomposite, we use a porous, insulating ceramic substrate for operando X-ray scattering. The ceramic substrate performs several functions: it serves as a reservoir of 1-ethyl-3-methylimidazolium bis(trifluoromethylsulfonyl)imide (EMIM:TFSI), acts as a suitable substrate for grazing-incidence scattering (minimal overlap with the OMIEC; Fig. 1 and Supplementary Fig. 1) and its insulating nature limits parasitic currents and side reactions during charging/discharging the OMIEC poly(2-(3,3′-bis(2-(2-(2-methoxyethoxy)ethoxy)ethoxy)-[2,2′-bithiophen]-5-yl) thieno [3,2-b]thiophene) (p(g2T-TT)) (Fig. 1b and Supplementary Fig. 2). This design enables high-quality electrochemical characterization to be performed on polymer thin films at synchrotron beamlines, demonstrated by the operando cyclic voltammogram (CV) shown in Fig. 1c.

On forming the nanocomposite by permeating p(g2T-TT) with EMIM:TFSI, the most conspicuous change is in the (100) peak, which corresponds to the lamellar stacking distance. This spacing expands by 5.3 Å (31%) due to EMIM:TFSI molecules spontaneously entering the side-chain lamellae. This expansion is commensurate with the ion dimensions[27]. Based on the swelling and molar volumes of the components, we estimate that there is on average one anion–cation pair per monomer in the mixed-conductor nanocomposite (Supplementary Table 1). Surprisingly, after the initial intercalation of ions into the polymer structure, electrochemical charging of the semiconductor does not result in significant expansions of the lamellar stacking distance; in fact, a modest contraction is observed (Supplementary Fig. 4). We, thus, attribute this contraction to cation expulsion needed to maintain charge neutrality of the nanocomposite following polymer oxidation. Notably, the restructuring of ionic-liquid-gated OMIEC materials greatly differ from aqueous systems, where hydrated anions entering the crystallites during electrochemical charging cause expansions of the (h00) planes[28]. Q7

We represent the evolution of the material's structure during the CV measurement in the form of a heat map where the scattering is collected every second and shown as a column of pixels (Fig. 2). By measuring the injected charge during the CV (Supplementary Fig. 5), the carrier density in the semiconductor can be quantitatively correlated to structural changes in the nanocomposite. The modulation of the (100) peak area is perfectly synchronized with the changes in the charge carrier density in the film (Fig. 2a), indicating that electrochemical doping is responsible for the observed changes (Supplementary Note 1) and highlighting the ideal reversibility of the ion insertion/expulsion processes. The (010) peak, corresponding to the π stacking of the rigid backbones, undergoes a modest contraction on charging (Fig. 2b). The π-stacking contraction appears to be the most rapid at lower carrier densities when the first charges are added and exhibits a minimal change towards the maximum carrier densities (and the most positive electrochemical potentials). The peak shift is also accompanied by small intensity increases, attributed to greater crystallinity due to the planarization of conjugated backbone units ensuing polaron formation.

To investigate electronic transport in the nanocomposite, we operate the film as the channel of an electrochemical transistor by patterning the source and drain electrodes on the insulating substrate (Fig. 3a). The electrochemical potential of the sample was varied relative to the reference electrode, whereas the conductivity was measured with a small (50 mV) bias between the source and drain[29]. Thus, differential and average carrier mobilities can be determined from conductivity changes following known increases in carrier density in the film (Fig. 3b). In agreement with CV measurements, the area of the lamellar stacking peak linearly increases with the carrier density, and the greatest contraction in the π-stacking distance occurs at potentials just above the threshold of the transistor, indicating that the initial

https://doi.org/10.1038/s41563-023-01476-6

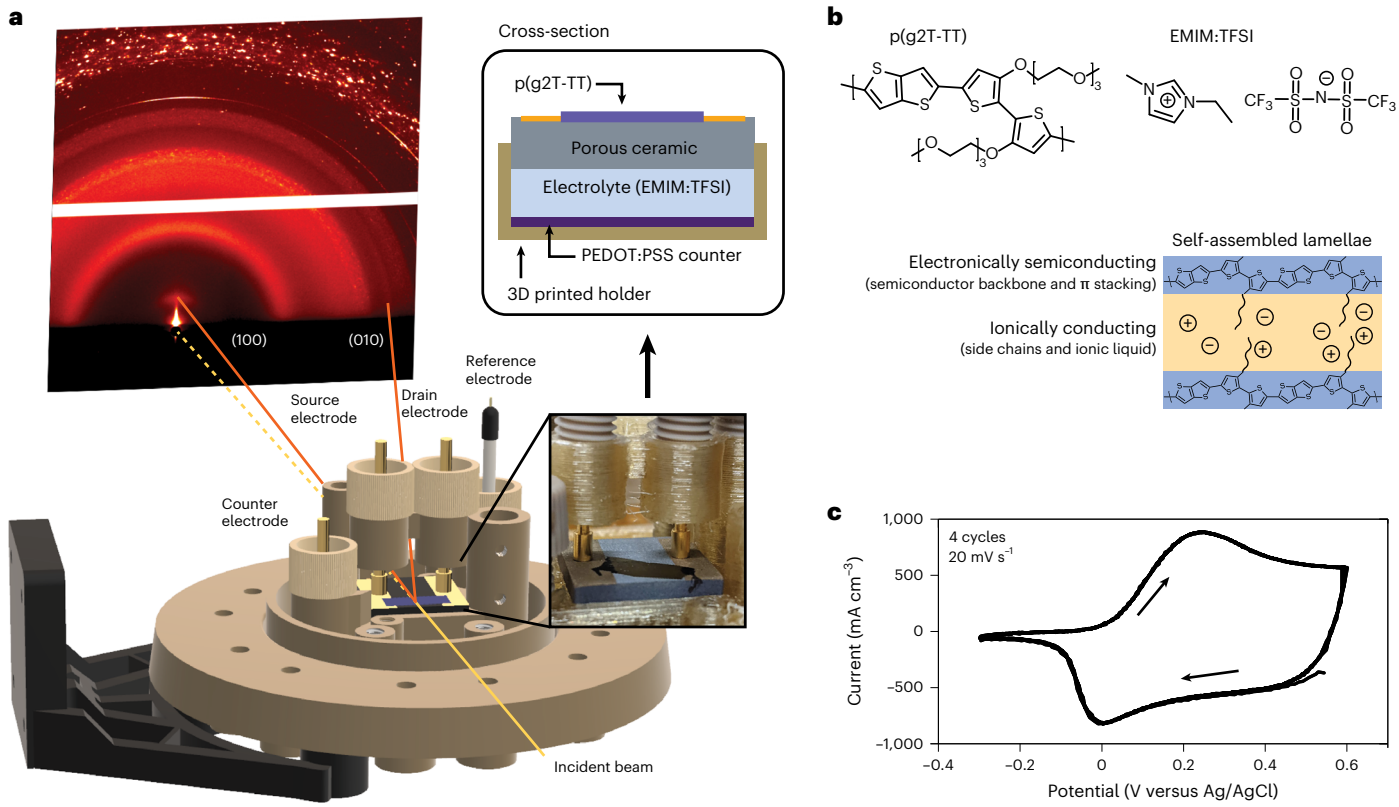

Fig. 1 | Characterization of the nanocomposite structure. a, Schematic of the electrochemical cell used for operando X-ray scattering measurements. **b**, Chemical structures of the components and schematic of the nanocomposite structure. **c**, CV of the system taken during operando X-ray characterization, with the scan direction shown by the arrows.

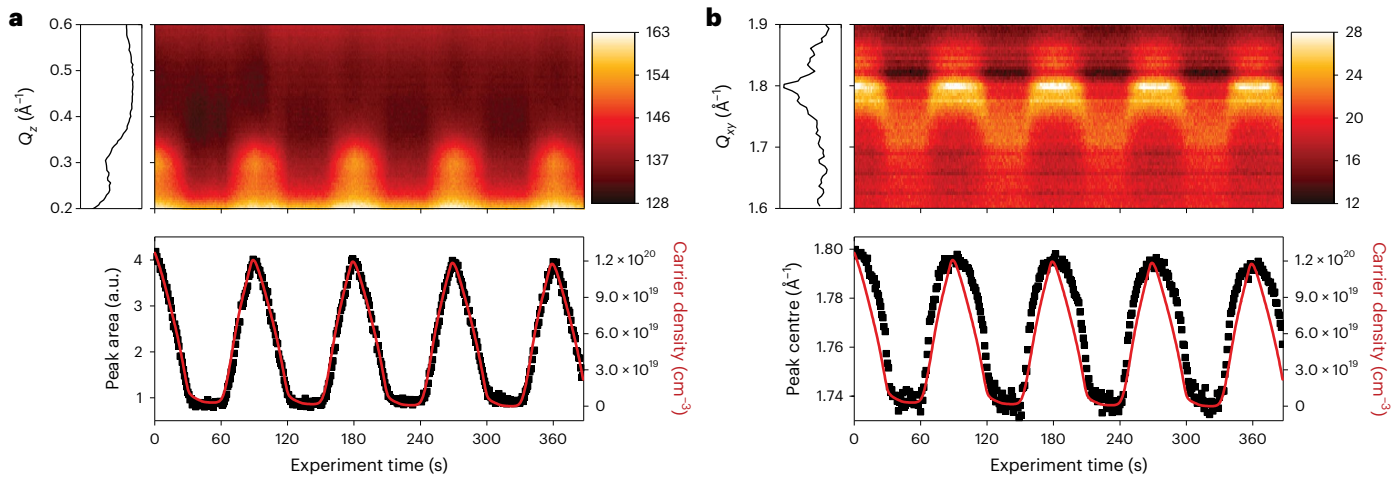

Fig. 2 | Structural evolution of the material under electrochemical charging. a,**b**, Lamellar-stacking peak area (**a**) and π-stacking peak centre (**b**) of p(g2T-TT) over the course of a CV. The scan rate was 20 mV s^{-1} and the potential range was from −0.3 to 0.6 V versus Ag/AgCl. The colour bar on the right of the heat maps displays the intensity scale used to show the peak changes during the experiment, and an initial scattering lineout is shown on the left. The fits were performed for each lineout and are shown in the bottom panel. The carrier density in the film throughout the duration of the CV, displayed in red, is overlaid with the relevant scattering fits.

carriers produce larger changes in the structure of the crystallites (Fig. 3c,d). The differential hole mobility reaches a peak at 0.3–0.4 V, which aligns well with the peak transconductance, confirming that this peak is governed by transport rather than capacitance[30]. Interestingly, the differential hole mobility peaks at a potential where the π stacking of the material shows minimal contraction on charging. The continued evolution of the (100) peak area indicates the charging of crystallites, but the addition of these high-mobility carriers do not result in significant π-stacking strains.

Evolution of polaron-induced ordering in the polymer

Operando X-ray scattering provides information about the structural transformations of crystallites on charging. Spectroelectrochemistry,

https://doi.org/10.1038/s41563-023-01476-6

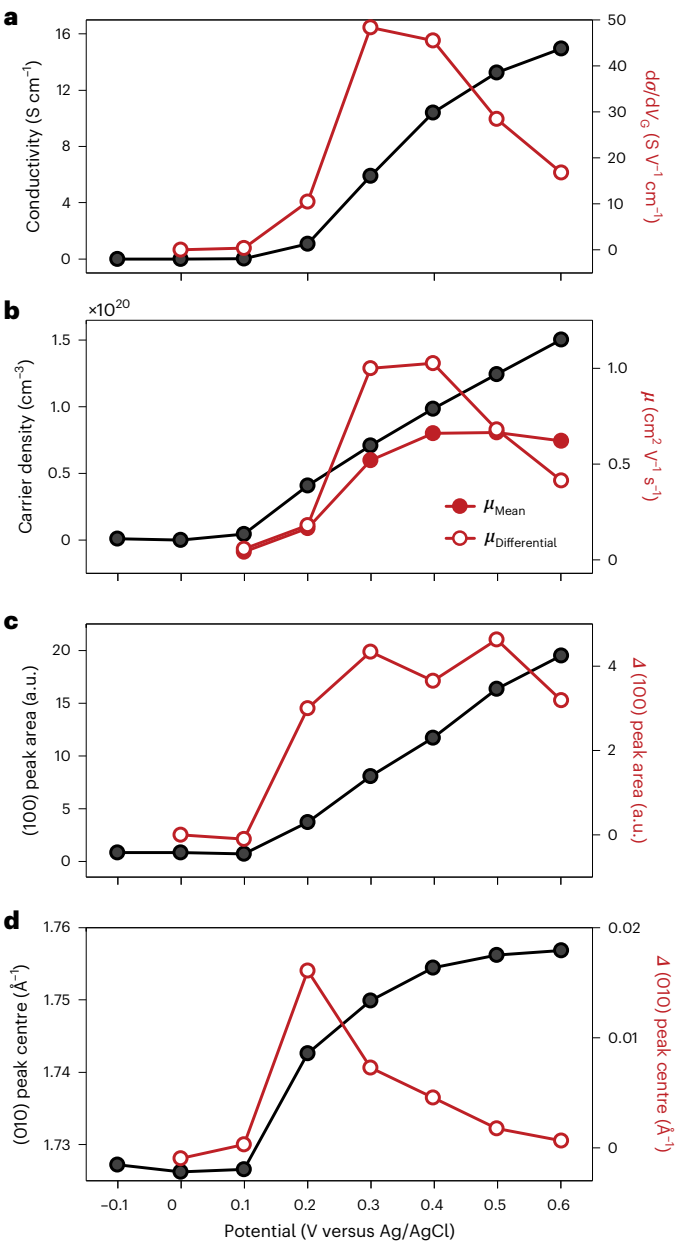

Fig. 3 | Operando OECT transfer curve. a, Conductivity (black) and dσ/dV_G (the conductivity analogue of transconductance) (red). **b**, Charge carrier density (black) and corresponding hole mobility (red). The 'differential' mobility (open symbols) is the mobility of newly added carriers at each potential step, given by $\Delta\sigma/(e\Delta\rho)$, whereas the 'mean' mobility (solid symbols) is the average mobility of all the carriers, given by $\sigma/(e\rho)$. **c**,**d**, Peak fits of the lamellar-stacking peak area (**c**) and π-stacking peak centre (**d**) are shown in black, and the relative changes from the previous electrochemical potential are shown in red. The film's electrochemical potential (*x* axis) is reported relative to an Ag/AgCl reference electrode.

on the other hand, reveals information about where the injected charges reside in the microstructure, for example, disordered regions versus aggregates, providing complementary information. To this end, we employ electrochemical charge modulation spectroscopy in the visible–near-infrared region to measure changes to both aggregate and amorphous absorption in p(g2T-TT). As the film potential is stepped from a neutral state to an oxidized state, the addition of charge carriers bleaches the π–π* absorption (Supplementary Fig. 6). The difference between the subsequent spectra is the absorption from the regions in the material where newly added charge carriers reside (Fig. 4a). Fitting the vibronic features of these differential spectra across a range of electrochemical potentials (Supplementary Note 2) provides insights into the local environment experienced by charge carriers at specific energies in the density of states. Indeed, the ratio of the oscillator strength of the first two vibronic features (the 0–0/0–1 ratio) is related to the relative amount of intrachain and interchain delocalization of excitons created on photoexcitation[31]. These exciton delocalization lengths are proxies for order: a chain with more intrachain order (more J-like) will lead to the formation of excitons that exhibit reduced interchain delocalization (less H-like)[32,33]. Hence, the degree of intrachain coupling has been taken as a measure of crystalline quality: a greater intrachain delocalization of the exciton is indicative of more ordered chains in higher-quality crystallites[34].

As the electrochemical potential is increased, the absorption of neutral (unbleached) aggregates in the film decreases steadily after the oxidation onset, as most (~84%) of the injected charge carriers go to aggregates rather than amorphous regions (Fig. 4b and Supplementary Fig. 7). As carriers are added deeper into the density of states, we find that newly added carriers populate increasingly J-like chains, as reported in poly(3-hexylthiophene) (ref. [35]). This is evidenced by a blueshift in E_{0-0}, as well as the 0–0/0–1 ratio that rises above unity[36,37]. Such changes are the characteristic of chains with planar backbones that allow for the intrachain delocalization of excitons[34,37]. The transition to populate more J-like aggregates coincides with an increase in the coherence length of the π-stacking peak, indicating increased order within the crystallites (Fig. 4b). Recall that the largest contraction in the π-stacking distance was observed at lower carrier densities (Fig. 3) when newly added carriers still populate the chains that possess considerable H-aggregate character and are thus more disordered. We conclude that these initial charge carriers result in chain straightening and planarization in lower-quality crystallites, which has two effects: (1) it decreases the π-stacking distance and (2) it increases the π-stacking coherence length, resulting in an overall enhancement in crystalline order. This change increases the mobility of the subsequent carriers as they populate aggregates with a more pronounced J-aggregate character since the chain-straightened crystallites possess higher intrachain order and longer conjugation lengths (Supplementary Note 3). Thus, we conclude that transport becomes more efficient at higher carrier densities because the initial carriers induce an intrachain order in the neighbouring chains, which increases the mobility of subsequent carriers.

Probing ion dynamics in the nanocomposite

To investigate the nature of ions located within the crystalline lamellae, we performed ^{1}H and ^{19}F pulsed-field gradient (PFG) nuclear magnetic resonance (NMR) spectroscopy to directly measure ion diffusion. Self-diffusion coefficients in the neat ionic liquid were measured at 25 °C and determined to be 5.6 and 3.4 × 10^{-7} cm^2 s^{-1} for the cation (EMIM$^+$) and anion (TFSI$^-$), respectively (Supplementary Fig. 8). Similar measurements were then performed on an oriented film of the nanocomposite to characterize the dynamics of ions confined between the semiconductor lamellae. An analysis of the diffusivity measurements by fitting attenuation data to the Stejskal–Tanner equation revealed two-component diffusion for both cation and anion (Supplementary Fig. 9)[38,39]. The diffusivities of the faster-diffusing components for both cation and anion match the values of the neat ionic liquid, which we attribute to excess ionic liquid on the surface or between the wrapped layers. The slower-diffusing component corresponds to an ionic liquid confined within the nanocomposite, which is highly mobile even at 25 °C (D_{EMIM} = 9.0 × 10^{-8} cm^2 s^{-1} and D_{TFSI} = 4.3 × 10^{-8} cm^2 s^{-1})[40]. In previous work, cation and anion diffusivities for an ionic liquid (PEt_4BF_4) confined within the carbon nanopores of a supercapacitor electrode were reduced by more than 100 times, with a strong dependence on pore size[41]. The larger characteristic spacing in this system (~2.2 nm) and

https://doi.org/10.1038/s41563-023-01476-6

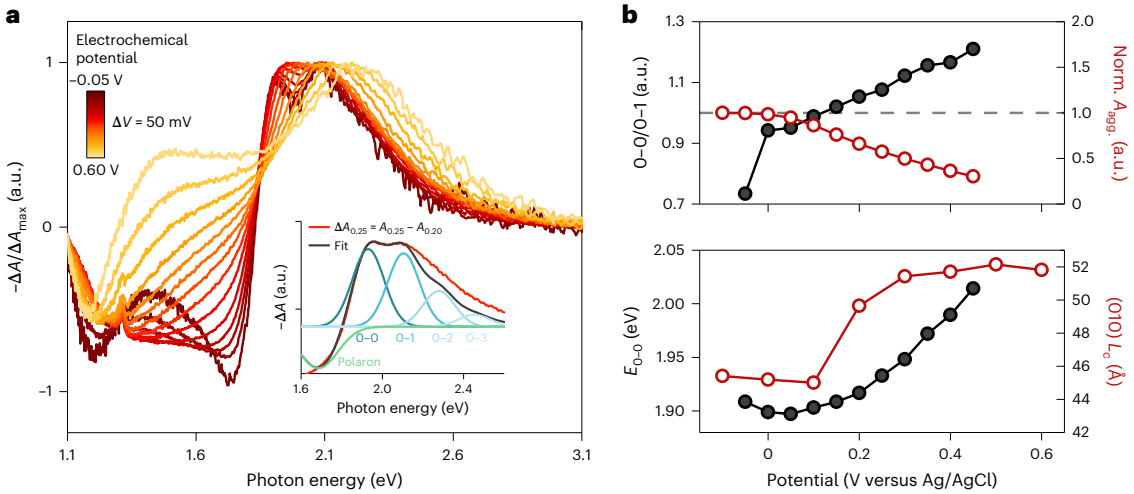

Fig. 4 | Electrochemical charge modulation spectroscopy. a, Differential visible–near-infrared absorption spectra at different electrochemical potentials (colour bar). The spectra were normalized to the bleaching of the π–π* transition for a qualitative comparison of the spectral shape. A representative fit of the charge-modulated spectra is shown in the inset, including polaron and vibronic (0–0, 0–1, 0–2, 0–3) absorptions. **b**, Results from fitting the differential spectra showing the 0–0/0–1 ratio for newly bleached chains (black) and the absorption of unbleached aggregates (red) normalized to the initial value (top). The 0–0 transition energy ($E_{0\text{–}0}$) (black) and coherence length (L_c) of the (010) scattering peak (red), taken from the operando transfer curve (bottom). Electrochemical potentials are reported relative to an Ag/AgCl reference electrode. The film's potential was stepped from −0.1 to 0.6 V versus Ag/AgCl in 50 mV steps, and the spectra and corresponding fits are reported at the endpoint of the potential step (inset).

interactions with the side chains probably contribute to the enhanced ion mobility, providing efficient ionic transport at room temperature even though, at most, only a few molecular layers of ionic liquid are present between each semiconductor sheet. We further note that semiconductor side-chain length (and thus lamellar spacing) can be synthetically designed, which offers intriguing opportunities to further enhance ionic transport in these materials.

Charge transport insights

We showed the formation of polymer/ionic liquid compounds that are promising materials at the nexus of electrochemistry and solid-state physics. Starting with a polymer that forms an ordered semicrystalline microstructure, we observe that the spontaneous infiltration of ionic liquid into polymer crystallites does not destroy the ordered microstructure. Such spontaneous swelling does not occur when non-polar alkyl side chains are used (Supplementary Fig. 10); therefore, ion insertion in such polymers produces significant structural pertubations that impose kinetic barriers[42,43]. Thus, the composite system we investigate here is unique in this respect, highlighting the modularity of synthetic design where independently designed backbones and side chains can be combined[44].

The complete permeation of the polymer with the ionic liquid has important consequences for both ion and electron transport. Because of the high ionic density within the crystallites, the insertion or expulsion of an ion during charging need not involve any long-range ionic motion or significant structural deformation. Indeed, this process can be viewed as the reversible formation of an 'ionic vacancy' or an 'ionic interstitial' in the already formed polymer/ionic liquid composite. This process can quickly occur by ion–ion interactions at the interface with the electrolyte or amorphous domains. The stabilization afforded by the large ion density combined with the material's nanostructured nature enables charge storage densities (~20 C cm^{-3}) that are orders of magnitude higher than other artificial mixed conductors[3]. Furthermore, since the ionic liquid mostly retains its liquid-like transport properties within the nanocomposite, these short-range diffusion processes can be fast, as corroborated by PFG NMR measurements. In this context, it has already been observed that artificial synapses made with our composites exhibit high-speed switching down to the nanosecond domain, not limited by fundamental materials properties but rather by device design[14]. This is a case where decreased ion-transit distances can lead to faster operation, as has been shown for internal-ion gated transistors[45]. This switching mechanism suggests that polymer/ionic-liquid composites hold great promise for fast-switching iontronic devices and beyond, thus realistically opening the optoelectronics space to electrochemical materials.

The lack of significant structural deformation, on the other hand, ensures that electronic transport is not impeded on ion intercalation. In fact, we find that hole mobility is high in these composites and that charging gives rise to a sharp increase in carrier transport. The explanation for such an observation is made possible by our multimodal study. We observe that the first carriers are introduced into crystallites with relatively disordered chains that form H-like aggregates. Interestingly, the relatively low carrier mobility observed in these conditions (~0.1 $cm^2 V^{-1} s^{-1}$) is similar to that observed in field-effect devices and indeed occurs at similar charge densities (~$1–2 \times 10^{19}$ cm^{-3}). The evidence of initial disorder of these chains is given by the π-stacking contraction on charging and subsequent increase in coherence length, where it is known that charged chains are straighter and thus prone to better packing. The high charge densities achievable by electrochemical gating enables populating of chains characterized by increased intrachain order in the crystallites. These more planar chains allow for higher mobility, up to 1 $cm^2 V^{-1} s^{-1}$, and their degree of order is such that the addition of charges no longer appreciably affects the π stacking. Thus, we conclude that the key to high mobility in this conjugated polymer is access to chains exhibiting more intrachain order. In electrochemical doping, these chains are dynamically created by the initial charge carriers. Although it is often stated that high-mobility polymers should exhibit the interchain delocalization of polarons, our results indicate that high mobility is dependent on efficient one-dimensional transport along single chains. Being able to modulate charge density with minimal structural changes makes this result unambiguous.

Outlook

In summary, we show that ionic liquids and conjugated polymers can spontaneously form nanostructured mixed conductors that exhibit reversible electrochemical doping and electronic transport

modulation. These composites exhibit efficient electronic and ionic transport at room temperature; they are effectively bulk mixed conductors due to the intimate contact between ionically and electronically conducting domains at the nanoscale. Using the multimodal characterization techniques developed here, we reveal that the addition of charge carriers induces subtle changes into polymer conformation within the crystallites. These changes enhance intrachain ordering, thereby increasing the mobility of subsequent carriers. Thus, such operando characterization allows us to uncover the mechanisms underlying the surprisingly high hole mobility observed in polymeric mixed conductors and the origin of the strong charge density dependence of transport. In a broader context, this electrochemically active nanocomposite offers exciting possibilities at the nexus of solid-state chemistry and electronics due to the ability to achieve fast and deep modulation up to high electronic carrier densities in the semiconductor lamellae. Combined with the ability to synthetically design both electronic and ionic domains of the nanocomposite, there exists a large design space for the synthesis of materials families exhibiting the fast modulation of a wide range of electronic, optical, thermal and even mechanical properties.

Online content

Any methods, additional references, Nature Portfolio reporting summaries, source data, extended data, supplementary information, acknowledgements, peer review information; details of author contributions and competing interests; and statements of data and code availability are available at https://doi.org/10.1038/s41563-023-01476-6.

References

1. Maier, J. Nanoionics: ion transport and electrochemical storage in confined systems. *Nat. Mater.* **4**, 805–815 (2005).
2. Bisri, S. Z., Shimizu, S., Nakano, M. & Iwasa, Y. Endeavor of iontronics: from fundamentals to applications of ion-controlled electronics. *Adv. Mater.* **29**, 1607054 (2017).
3. Chen, C. C., Fu, L. & Maier, J. Synergistic, ultrafast mass storage and removal in artificial mixed conductors. *Nature* **536**, 159–164 (2016).
4. Sata, N., Eberman, K., Eberl, K. & Maier, J. Mesoscopic fast ion conduction in nanometre-scale planar heterostructures. *Nature* **408**, 946–949 (2000).
5. Casado, N. et al. Tuning electronic and ionic conductivities in composite materials for electrochemical devices. *ACS Appl. Polym. Mater.* **3**, 1777–1784 (2021).
6. del Olmo, R., Mendes, T. C., Forsyth, M. & Casado, N. Mixed ionic and electronic conducting binders containing PEDOT:PSS and organic ionic plastic crystals toward carbon-free solid-state battery cathodes. *J. Mater. Chem. A* **10**, 19777–19786 (2022).
7. Olmo, R., Del, Casado, N., Olmedo-Martínez, J. L., Wang, X. & Forsyth, M. Mixed ionic-electronic conductors based on PEDOT:PolyDADMA and organic ionic plastic crystals. *Polymers* **12**, 1981 (2020).
8. Chen, H. et al. Exploring chemical, mechanical, and electrical functionalities of binders for advanced energy-storage devices. *Chem. Rev.* **118**, 8936–8982 (2018).
9. Lopez, J., Mackanic, D. G., Cui, Y. & Bao, Z. Designing polymers for advanced battery chemistries. *Nat. Rev. Mater.* **4**, 312–330 (2019).
10. Tan, S. T. M. et al. Redox-active polymers designed for the circular economy of energy storage devices. *ACS Energy Lett.* **6**, 3450–3457 (2021).
11. Cea, C. et al. Enhancement-mode ion-based transistor as a comprehensive interface and real-time processing unit for in vivo electrophysiology. *Nat. Mater.* **19**, 679–686 (2020).
12. Tuchman, Y., Quill, T. J., LeCroy, G. & Salleo, A. A stacked hybrid organic/inorganic electrochemical random-access memory for scalable implementation. *Adv. Electron. Mater.* **8**, 2100426 (2021).
13. Paulsen, B. D., Tybrandt, K., Stavrinidou, E. & Rivnay, J. Organic mixed ionic–electronic conductors. *Nat. Mater.* **19**, 13–26 (2020).
14. Melianas, A. et al. Temperature-resilient solid-state organic artificial synapses for neuromorphic computing. *Sci. Adv.* **6**, eabb2958 (2020).
15. Lei, Z., Chen, B., Koo, Y. M. & Macfarlane, D. R. Introduction: ionic liquids. *Chem. Rev.* **117**, 6633–6635 (2017).
16. Wu, X. et al. Ionic-liquid doping enables high transconductance, fast response time, and high ion sensitivity in organic electrochemical transistors. *Adv. Mater.* **31**, 1805544 (2019).
17. Wu, X. et al. Ionic-liquid induced morphology tuning of PEDOT:PSS for high-performance organic electrochemical transistors. *Adv. Funct. Mater.* **32**, 2108510 (2022).
18. Quill, T. J. et al. Ion pair uptake in ion gel devices based on organic mixed ionic–electronic conductors. *Adv. Funct. Mater.* **31**, 2104301 (2021).
19. Hou, Y. & Hou, X. Bioinspired nanofluidic iontronics. *Science* **373**, 628–629 (2021).
20. Chun, H. & Chung, T. D. Iontronics. *Annu. Rev. Anal. Chem.* **8**, 441–462 (2015).
21. Bischak, C. G. et al. A reversible structural phase transition by electrochemically-driven ion injection into a conjugated polymer. *J. Am. Chem. Soc.* **142**, 7434–7442 (2020).
22. Thomas, E. M. et al. X-ray scattering reveals ion-induced microstructural changes during electrochemical gating of poly(3-hexylthiophene). *Adv. Funct. Mater.* **28**, 1803687 (2018).
23. Paulsen, B. D. et al. Electrochemistry of thin films with in situ/operando grazing incidence X-ray scattering: bypassing electrolyte scattering for high fidelity time resolved studies. *Small* **17**, 2103213 (2021).
24. Flagg, L. Q. et al. In situ studies of the swelling by an electrolyte in electrochemical doping of ethylene glycol-substituted polythiophene. *ACS Appl. Mater. Interfaces* **14**, 29052–29060 (2022).
25. Thelen, J. L. et al. Relationship between mobility and lattice strain in electrochemically doped poly(3-hexylthiophene). *ACS Macro Lett.* **4**, 1386–1391 (2015).
26. Zhang, S., Beach, E., Anastas, P. T., Pfefferle, L. D. & Osuji, C. O. Self-assembly of supramolecular complexes of charged conjugated polymers and imidazolium-based ionic liquid crystals. *Giant* **9**, 100088 (2022).
27. Largeot, C. et al. Relation between the ion size and pore size for an electric double-layer capacitor. *J. Am. Chem. Soc.* **130**, 2730–2731 (2008).
28. Cendra, C. et al. Role of the anion on the transport and structure of organic mixed conductors. *Adv. Funct. Mater.* **29**, 1807034 (2019).
29. Hulea, I. N. et al. Wide energy-window view on the density of states and hole mobility in poly(*p*-phenylene vinylene). *Phys. Rev. Lett.* **93**, 166601 (2004).
30. Friedlein, J. T. et al. Influence of disorder on transfer characteristics of organic electrochemical transistors. *Appl. Phys. Lett.* **111**, 023301 (2017).
31. Chang, X., Balooch Qarai, M. & Spano, F. C. HJ-aggregates of donor–acceptor–donor oligomers and polymers. *J. Chem. Phys.* **155**, 034905 (2021).
32. Clark, J., Silva, C., Friend, R. H. & Spano, F. C. Role of intermolecular coupling in the photophysics of disordered organic semiconductors: aggregate emission in regioregular polythiophene. *Phys. Rev. Lett.* **98**, 206406 (2007).
33. Spano, F. C. Modeling disorder in polymer aggregates: the optical spectroscopy of regioregular poly(3-hexylthiophene) thin films. *J. Chem. Phys.* **122**, 234701 (2005).
34. Clark, J., Chang, J. F., Spano, F. C., Friend, R. H. & Silva, C. Determining exciton bandwidth and film microstructure in

polythiophene films using linear absorption spectroscopy. *Appl. Phys. Lett.* **94**, 163306 (2009).
35. Harris, J. K., Neelamraju, B. & Ratcliff, E. L. Intersystem subpopulation charge transfer and conformational relaxation preceding in situ conductivity in electrochemically doped poly(3-hexylthiophene) electrodes. *Chem. Mater.* **31**, 6870–6879 (2019).
36. Brown, P. J. et al. Effect of interchain interactions on the absorption and emission of poly(3-hexylthiophene). *Phys. Rev. B* **67**, 064203 (2003).
37. Spano, F. C. & Silva, C. H- and J-aggregate behavior in polymeric semiconductors. *Annu. Rev. Phys. Chem.* **65**, 477–500 (2014).
38. Stejskal, E. O. & Tanner, J. E. Spin diffusion measurements: spin echoes in the presence of a time-dependent field gradient. *J. Chem. Phys.* **42**, 288–292 (1965).
39. Sinnaeve, D. The Stejskal–Tanner equation generalized for any gradient shape—an overview of most pulse sequences measuring free diffusion. *Concepts Magn. Reson.* **40A**, 39–65 (2012).
40. Hoarfrost, M. L., Tyagi, M. S., Segalman, R. A. & Reimer, J. A. Effect of confinement on proton transport mechanisms in block copolymer/ionic liquid membranes. *Macromolecules* **45**, 3112–3120 (2012).
41. Forse, A. C. et al. Direct observation of ion dynamics in supercapacitor electrodes using in situ diffusion NMR spectroscopy. *Nat. Energy* **2**, 16216 (2017).
42. Guardado, J. O. & Salleo, A. Structural effects of gating poly(3-hexylthiophene) through an ionic liquid. *Adv. Funct. Mater.* **27**, 1701791 (2017).
43. Lee, J. et al. Ion gel-gated polymer thin-film transistors: operating mechanism and characterization of gate dielectric capacitance, switching speed, and stability. *J. Phys. Chem. C* **113**, 8972–8981 (2009).
44. Bronstein, H., Nielsen, C. B., Schroeder, B. C. & McCulloch, I. The role of chemical design in the performance of organic semiconductors. *Nat. Rev. Chem.* **4**, 66–77 (2020).
45. Spyropoulos, G. D., Gelinas, J. N. & Khodagholy, D. Internal ion-gated organic electrochemical transistor: a building block for integrated bioelectronics. *Sci. Adv.* **5**, eaau7378 (2020).

Methods

Cell fabrication

The operando cell was designed using Fusion360 (Autodesk) and printed from 3DX-TECH PEKK-A on an Intamsys Funmat HT printer. The entrance and exit windows of the cell consisted of 8 µm aluminium foils (MTI Corporation) and were sealed with Kapton tape. The scattering from these windows is at sufficiently high q such that no scattering overlaps with the areas of interest. Kapton tape was used to seal any openings and to provide optical access during alignment.

Substrate preparation

Porous ceramic substrates (Newark) were cleaned in acetone and polished by hand using diamond lapping paper (McMaster-Carr). Gold contacts were evaporated onto the frits using a thermal evaporator in a nitrogen glovebox.

Film transfer: p(g2T-TT), synthesized as previously reported[46], was dissolved in chloroform (1 mg ml^{-1}) and blade coated on a Si wafer coated with a poly(diallyldimethylammonium bis(trifluoromethanesulfonyl) imide) (polyDADMAC TFSI) lift-off layer (spun at 1,000 rpm; 10 mg ml^{-1}). The blade-coated film was lifted off the Si substrate in acetone and transferred to the porous ceramic.

Operando X-ray scattering

Grazing-incidence wide-angle X-ray scattering measurements of p(g2T-TT) were performed at the Stanford Synchrotron Radiation Lightsource on beamline 10-2 using an incident photon energy of 12 keV using a focused beam approximately 50 µm in height. An EIGER 1M detector was mounted on a 2θ arm at a distance of 152 mm away from the sample at an angle of 10°. The measurements were taken at an incident angle of 0.5° at ambient temperature. The out-of-plane (Q_z) and in-plane (Q_{xy}) lineouts were taken from cake slices from $\chi = -20°$ to 20° and 60° to 87° with respect to the Q_z direction, respectively. Small-angle scattering between $\chi = -5°$ and 5° was excluded from the out-of-plane lineouts. The peaks were fit to Gaussian–Lorentzian lineshapes using the lmfit package in Python. To isolate the π-stacking peak for fitting, out-of-plane lineouts were subtracted from the in-plane lineouts to remove the isotropic scattering from the substrate. The X-ray scattering data were reduced in Python using the open-source pyFAI and pygix modules[47,48]. A forked version of the pygix module was used (available at https://github.com/ctakacs/pygix) for compatibility with Python 3.

Operando electrochemistry

Electrochemical measurements were taken on a two-channel Biologic SP-300 potentiostat in a three-electrode setup with a leakless Ag/AgCl reference electrode (eDAQ) and a poly(3,4-ethylenedioxythiophene) polystyrene sulfonate (Clevios PH1000) counter electrode. EMIM:TFSI (Iolitec) was stored in a nitrogen glovebox before use. Poly(3,4-ethylenedioxythiophene) polystyrene sulfonate was prepared as previously described[14] and drop casted on a conductive carbon paper (P75, Fuel Cell Store) to form a high-capacitance counter electrode. The CV experiments were performed on unpatterned ceramic substrates, or by connecting the source and drain electrodes of a patterned substrate to the working electrode of the potentiostat. Operando transistor measurements were performed by separately biasing the source and drain electrodes using the dual-channel potentiostat as a bipotentiostat, still in a three-electrode setup (namely, with separate counter and reference electrodes). The carrier density was calculated from the injected charge over the course of the CV or transfer curve and film volume. The thicknesses were measured after the experiments were performed and thus correspond to the swollen state of the material.

Electrochemical charge modulation spectroscopy

Spectroelectrochemical measurements were performed using a home-built spectrometer with an Ocean Optics light source (tungsten–halogen light source) and detector (Red Tide). A quartz cuvette with a 3D-printed holder was used to conduct measurements in the transmission mode. The cuvette was capped with a 3D-printed cap and purged with argon to remove ambient oxygen. Films were spun from chloroform onto indium-tin-oxide-coated glass substrates (1,000 rpm; 5 mg ml^{-1}). An Ivium CompactStat potentiostat was used to control the electrochemical potential of the p(g2T-TT) film in a three-electrode configuration (chronoamperometry) using identical counter and reference electrodes described above. The electrochemical potential of the film (working electrode) was increased in 50 mV steps, and the difference between the subsequent absorption spectra gives the charge-modulated spectra, which was then fit to the Spano model[31]. Details regarding the fitting of the spectra can be found in Supplementary Note 2.

NMR measurements

The ^{1}H and ^{19}F PFG NMR experiments, characterizing cation (EMIM$^+$) and anion (TFSI$^-$) self-diffusion, respectively, were performed at a field strength of 9.4 T using a 400 MHz Bruker NEO spectrometer and a Bruker 5 mm water-cooled double-resonance broadband diffusion probe, which was equipped with z-axis gradient capabilities permitting a maximum gradient strength of 17 T m^{-1} and variable-temperature control. A standard stimulated-echo sequence using sine-bell magnetic-field gradient pulses was employed, where only the gradient strength was varied for each measurement; spoiler gradient pulses of 2 ms and a longitudinal eddy-current delay period of 20 ms were used for all the experiments. Additionally, dummy gradient pulses were performed before the first spectral acquisition. Neat EMIM:TFSI was loaded and measured in a standard 5 mm NMR tube (Wilmad). The p(g2T-TT) sample was first drop cast from solution onto a sacrificial layer, as described above. The film (comprising ~1 mg of material) was then transferred and rolled onto a coaxial NMR insert (Wilmad) to orient the lamellae of the polymer along the PFG axis (z axis). Ionic liquid was introduced into the film via dip coating in a solution of EMIM:TFSI, and the excess surface liquid was removed via a Kimwipe. The insert was then placed in a standard 5 mm NMR tube for PFG NMR measurements. Typical ^{1}H and ^{19}F PFG parameters, such as gradient pulse length (δ), diffusion time (Δ) and maximum gradient strength (g) for the neat ionic liquid (EMIM:TFSI) were as follows: $\delta = 2$ ms, $\Delta = 20$ ms, $g = 4$ T m^{-1} (^{1}H); $\delta = 2$ ms, $\Delta = 20$ ms, $g = 5$ T m^{-1} (^{19}F). Typical ^{1}H and ^{19}F PFG parameters for the p(g2T-TT) sample were as follows: $\delta = 2.5$ ms, $\Delta = 8.0$ ms, $g = 15.3$ T m^{-1} (^{1}H); $\delta = 1.5$ ms, $\Delta = 20.0$ ms, $g = 12.0$ T m^{-1} (^{19}F). All the measurements were performed at a calibrated sample temperature of 25 °C. Temperature and PFG strength calibrations were performed with a standard consisting of 80% ethylene glycol in DMSO-d6 (Cambridge Isotope Labs). Data were processed and analysed in Bruker TopSpin 4.1 and Bruker Dynamics Center.

Reporting summary

Further information on research design is available in the Nature Portfolio Reporting Summary linked to this article.

Data availability

All the data supporting the findings of this study are available within the Article, its Supplementary Information or from the corresponding authors upon request. Source data are provided with this paper.

References

46. Giovannitti, A. et al. Controlling the mode of operation of organic transistors through side-chain engineering. *Proc. Natl Acad. Sci. USA* **113**, 12017–12022 (2016).
47. Ashiotis, G. et al. The fast azimuthal integration Python library: pyFAI. *J. Appl. Crystallogr.* **48**, 510–519 (2015).
48. Dane, T. G. pygix. *GitHub* https://github.com/tgdane/pygix (2017).

Acknowledgements

We thank L. Richter for helpful discussions regarding X-ray scattering results, and E. Barks for assistance with ceramic polishing. T.J.Q. and G.L. acknowledge support from the National Science Foundation Graduate Research Fellowship Program under grant DGE-1656518. This material is based on work supported by the US Department of Energy (DOE), Office of Science, Office of Workforce Development for Teachers and Scientists, Office of Science Graduate Student Research (SCGSR) program. The SCGSR program is administered by the Oak Ridge Institute for Science and Education for the DOE under contract no. DE-SC0014664. A.G. and A.S. acknowledge funding from the TomKat Center for Sustainable Energy at Stanford University. A.S. gratefully acknowledges financial support from the National Science Foundation award no. DMR 1808401. The use of Stanford Synchrotron Radiation Lightsource, SLAC National Accelerator Laboratory, is supported by the US DOE, Office of Science, Office of Basic Energy Sciences, under contract no. DE-AC02-76SF00515. Part of this work was performed at the Stanford Nano Shared Facilities (SNSF), supported by the National Science Foundation under award ECCS-2026822. A.S. and T.J.Q. acknowledge financial support from the National Science Foundation and the Semiconductor Research Corporation, E2CDA award no. 1739795. We thank H. Celik and UC Berkeley's NMR facility in the College of Chemistry (CoC-NMR) for spectroscopic assistance; the instrument used in this work is supported by the National Science Foundation under grant no. 2018784. D.M.H. acknowledges support from the Joint Center for Energy Storage Research, an Energy Innovation Hub funded by the US DOE, Office of Science, Basic Energy Sciences.

Author contributions

T.J.Q., C.J.T., A.S. and A.G. conceived the study. T.J.Q. and C.J.T. performed the operando X-ray scattering experiments and analysed the data. T.J.Q. and G.L. carried out the spectroscopic measurements and G.L. performed the exciton fitting. D.M.H. performed the PFG NMR measurements under the supervision of J.A.R. and N.P.B. R.S. synthesized p(g2T-TT) under the supervision of I.M. T.J.Q., A.G. and A.S. wrote the manuscript and all the authors contributed to manuscript preparation and editing.

Competing interests

The authors declare no competing interests.

Additional information

Supplementary information The online version contains supplementary material available at https://doi.org/10.1038/s41563-023-01476-6.

Correspondence and requests for materials should be addressed to Alexander Giovannitti, Alberto Salleo or Christopher J. Takacs.

Peer review information *Nature Materials* thanks Magnus Berggren and the other, anonymous, reviewer(s) for their contribution to the peer review of this work.

QUERY FORM

Manuscript ID	**[Art. Id: 1476]**
Author	**Tyler J. Quill**

AUTHOR:

The following queries have arisen during the editing of your manuscript. Please answer by making the requisite corrections directly in the e.proofing tool rather than marking them up on the PDF. This will ensure that your corrections are incorporated accurately and that your paper is published as quickly as possible.

Query No.	*Nature of Query*
Q1:	Please check your article carefully, coordinate with any co-authors and enter all final edits clearly in the eproof, remembering to save frequently. Once corrections are submitted, we cannot routinely make further changes to the article.
Q2:	Note that the eproof should be amended in only one browser window at any one time; otherwise changes will be overwritten.
Q3:	Author surnames have been highlighted. Please check these carefully and adjust if the first name or surname is marked up incorrectly. Note that changes here will affect indexing of your article in public repositories such as PubMed. Also, carefully check the spelling and numbering of all author names and affiliations, and the corresponding email address(es).
Q4:	You cannot alter accepted Supplementary Information files except for critical changes to scientific content. If you do resupply any files, please also provide a brief (but complete) list of changes. If these are not considered scientific changes, any altered Supplementary files will not be used, only the originally accepted version will be published.
Q5:	Please check Figures for accuracy as they have been relabelled. Please markup minor changes in the eProof. For major changes, please provide revised figures. (Please note that in the eProof the figure resolution will appear at lower resolution than in the pdf and html versions of your paper.)
Q6:	If applicable, please ensure that any accession codes and datasets whose DOIs or other identifiers are mentioned in the paper are scheduled for public release as soon as possible, we recommend within a few days of submitting your proof, and update the database record with publication details from this article once available.
Q7:	Please note, we reserve 'significant' and its derivatives for statistical significance. Please reword where this is not the intended meaning (for example to important, notable, substantial); there are five instances throughout your text.
Q8:	In the title of Fig. 3, please use the full form of 'OECT'.
Q9:	In the sentence beginning 'The scattering from these windows is at...', please define 'q'.

QUERY FORM

Manuscript ID	**[Art. Id: 1476]**
Author	**Tyler J. Quill**

AUTHOR:

The following queries have arisen during the editing of your manuscript. Please answer by making the requisite corrections directly in the e.proofing tool rather than marking them up on the PDF. This will ensure that your corrections are incorporated accurately and that your paper is published as quickly as possible.

Query No.	*Nature of Query*
Q10:	For the sentence beginning 'The peaks were fit to Gaussian–Lorentzian lineshapes...', please provide the version number of Python, if available.

nature portfolio

Corresponding author(s): Giovannitti, A.; Salleo, A.;Takacs, C.

Last updated by author(s): Jan 4, 2023

Reporting Summary

Nature Portfolio wishes to improve the reproducibility of the work that we publish. This form provides structure for consistency and transparency in reporting. For further information on Nature Portfolio policies, see our Editorial Policies and the Editorial Policy Checklist.

Statistics

For all statistical analyses, confirm that the following items are present in the figure legend, table legend, main text, or Methods section.

n/a	Confirmed	
☒	☐	The exact sample size (*n*) for each experimental group/condition, given as a discrete number and unit of measurement
☐	☒	A statement on whether measurements were taken from distinct samples or whether the same sample was measured repeatedly
☒	☐	The statistical test(s) used AND whether they are one- or two-sided *Only common tests should be described solely by name; describe more complex techniques in the Methods section.*
☒	☐	A description of all covariates tested
☒	☐	A description of any assumptions or corrections, such as tests of normality and adjustment for multiple comparisons
☒	☐	A full description of the statistical parameters including central tendency (e.g. means) or other basic estimates (e.g. regression coefficient) AND variation (e.g. standard deviation) or associated estimates of uncertainty (e.g. confidence intervals)
☒	☐	For null hypothesis testing, the test statistic (e.g. *F*, *t*, *r*) with confidence intervals, effect sizes, degrees of freedom and *P* value noted *Give P values as exact values whenever suitable.*
☒	☐	For Bayesian analysis, information on the choice of priors and Markov chain Monte Carlo settings
☒	☐	For hierarchical and complex designs, identification of the appropriate level for tests and full reporting of outcomes
☒	☐	Estimates of effect sizes (e.g. Cohen's *d*, Pearson's *r*), indicating how they were calculated

Our web collection on statistics for biologists contains articles on many of the points above.

Software and code

Policy information about availability of computer code

Data collection	Electrochemical data was collected using commercially available EC-Lab v11.43 and IviumSoft v4.952 software. X-ray scattering collection was performed with commercially available spec software. The Vis-NIR spectrometer (OceanOptics QEPro) was controlled via MATLAB 2019b using commercially available OceanOptics drivers. NMR measurements were collected using Bruker TopSpin 4.1.
Data analysis	X-ray scattering data was reduced and analyzed using PyFAI and pygix open source libraries. Lineouts were fit using the open source lmfit library. Vis-NIR spectroscopy data was analyzed and fit using commercially available MATLAB 2020b software using the lsqnonlin fit function. NMR data was analyzed and fit using Bruker TopSpin 4.1 and Bruker Dynamics Center.

For manuscripts utilizing custom algorithms or software that are central to the research but not yet described in published literature, software must be made available to editors and reviewers. We strongly encourage code deposition in a community repository (e.g. GitHub). See the Nature Portfolio guidelines for submitting code & software for further information.

Data

Policy information about availability of data

All manuscripts must include a data availability statement. This statement should provide the following information, where applicable:

- Accession codes, unique identifiers, or web links for publicly available datasets
- A description of any restrictions on data availability
- For clinical datasets or third party data, please ensure that the statement adheres to our policy

The All the data that supportsupporting the findings of this study are available within the article, its Supplementary Information, or from the corresponding authors upon reasonable request. Source data are provided with this paper.

Human research participants

Policy information about studies involving human research participants and Sex and Gender in Research.

Reporting on sex and gender	*Use the terms sex (biological attribute) and gender (shaped by social and cultural circumstances) carefully in order to avoid confusing both terms. Indicate if findings apply to only one sex or gender; describe whether sex and gender were considered in study design whether sex and/or gender was determined based on self-reporting or assigned and methods used. Provide in the source data disaggregated sex and gender data where this information has been collected, and consent has been obtained for sharing of individual-level data; provide overall numbers in this Reporting Summary. Please state if this information has not been collected. Report sex- and gender-based analyses where performed, justify reasons for lack of sex- and gender-based analysis.*
Population characteristics	*Describe the covariate-relevant population characteristics of the human research participants (e.g. age, genotypic information, past and current diagnosis and treatment categories). If you filled out the behavioural & social sciences study design questions and have nothing to add here, write "See above."*
Recruitment	*Describe how participants were recruited. Outline any potential self-selection bias or other biases that may be present and how these are likely to impact results.*
Ethics oversight	*Identify the organization(s) that approved the study protocol.*

Note that full information on the approval of the study protocol must also be provided in the manuscript.

Field-specific reporting

Please select the one below that is the best fit for your research. If you are not sure, read the appropriate sections before making your selection.

☒ Life sciences ☐ Behavioural & social sciences ☐ Ecological, evolutionary & environmental sciences

For a reference copy of the document with all sections, see nature.com/documents/nr-reporting-summary-flat.pdf

Life sciences study design

All studies must disclose on these points even when the disclosure is negative.

Sample size	No sample size considerations were performed.
Data exclusions	No data were excluded from the study.
Replication	X-ray scattering measurements were repeated on different spots of the samples.
Randomization	Randomization not relevant.
Blinding	Blinding not relevant.

Reporting for specific materials, systems and methods

We require information from authors about some types of materials, experimental systems and methods used in many studies. Here, indicate whether each material, system or method listed is relevant to your study. If you are not sure if a list item applies to your research, read the appropriate section before selecting a response.

Materials & experimental systems

n/a	Involved in the study
☒	☐ Antibodies
☒	☐ Eukaryotic cell lines
☒	☐ Palaeontology and archaeology
☒	☐ Animals and other organisms
☒	☐ Clinical data
☒	☐ Dual use research of concern

Methods

n/a	Involved in the study
☒	☐ ChIP-seq
☒	☐ Flow cytometry
☒	☐ MRI-based neuroimaging